Characterization of Multipartite Entanglement for One Photon Shared Among Four Optical Modes

Scott B. Papp, *et al.*

Science **324**, 764 (2009);
DOI: 10.1126/science.1172260

Science (print ISSN 0036-8075; online ISSN 1095-9203) is published weekly, except the last week in December, by the American Association for the Advancement of Science, 1200 New York Avenue NW, Washington, DC 20005.

18. M. N. Shadlen, W. T. Newsome, *J. Neurophysiol.* **86**, 1916 (2001).
19. J. D. Roitman, M. N. Shadlen, *J. Neurosci.* **22**, 9475 (2002).
20. R. Kiani, T. D. Hanks, M. N. Shadlen, *J. Neurosci.* **28**, 3017 (2008).
21. A. K. Churchland, R. Kiani, M. N. Shadlen, *Nat. Neurosci.* **11**, 693 (2008).
22. J. M. Beck *et al.*, *Neuron* **60**, 1142 (2008).
23. J. I. Gold, M. N. Shadlen, *Trends Cogn. Sci.* **5**, 10 (2001).
24. T. Yang, M. N. Shadlen, *Nature* **447**, 1075 (2007).
25. Materials and methods are available as supporting material on *Science* Online.
26. N. Persaud, P. McLeod, A. Cowey, *Nat. Neurosci.* **10**, 257 (2007).
27. W. E. Shields, J. D. Smith, D. A. Washburn, *J. Exp. Psychol. Gen.* **126**, 147 (1997).
28. N. Kornell, L. K. Son, H. S. Terrace, *Psychol. Sci.* **18**, 64 (2007).
29. C. L. Colby, M. E. Goldberg, *Annu. Rev. Neurosci.* **22**, 319 (1999).
30. J. W. Gnadt, R. A. Andersen, *Exp. Brain Res.* **70**, 216 (1988).
31. M. L. Platt, P. W. Glimcher, *J. Neurophysiol.* **78**, 1574 (1997).
32. The activity of each neuron was normalized to the average response in the 300 ms preceding the motion, that is, the period after the appearance of the direction choice targets in the RF.
33. A. J. Parker, W. T. Newsome, *Annu. Rev. Neurosci.* **21**, 227 (1998).
34. E. Zohary, M. N. Shadlen, W. T. Newsome, *Nature* **370**, 140 (1994).
35. M. N. Shadlen, K. H. Britten, W. T. Newsome, J. A. Movshon, *J. Neurosci.* **16**, 1486 (1996).
36. The buildup rate on each trial was calculated by fitting a line to the neural activity in a ~300-ms window starting at the dip of activity after motion onset (*25*).
37. E. P. Cook, J. H. Maunsell, *Nat. Neurosci.* **5**, 985 (2002).
38. D. P. Hanes, J. D. Schall, *Science* **274**, 427 (1996).
39. J. Palmer, A. C. Huk, M. N. Shadlen, *J. Vis.* **5**, 376 (2005).
40. D. Vickers, J. Packer, *Acta Psychol. (Amst.)* **50**, 179 (1982).
41. W. J. Ma, J. M. Beck, P. E. Latham, A. Pouget, *Nat. Neurosci.* **9**, 1432 (2006).
42. The activity of each neuron was normalized by its (visual) response in the 300 ms after T_s onset.
43. J. W. Bisley, M. E. Goldberg, *Science* **299**, 81 (2003).
44. J. N. Kim, M. N. Shadlen, *Nat. Neurosci.* **2**, 176 (1999).
45. J. D. Smith, M. J. Beran, J. J. Couchman, M. V. Coutinho, *Psychon. Bull. Rev.* **15**, 679 (2008).
46. M. Watanabe, *Nature* **382**, 629 (1996).
47. A. Izquierdo, R. K. Suda, E. A. Murray, *J. Neurosci.* **24**, 7540 (2004).
48. R. Kawagoe, Y. Takikawa, O. Hikosaka, *Nat. Neurosci.* **1**, 411 (1998).
49. M. I. Leon, M. N. Shadlen, *Neuron* **24**, 415 (1999).
50. L. Tremblay, W. Schultz, *Nature* **398**, 704 (1999).
51. J. D. Wallis, E. K. Miller, *Eur. J. Neurosci.* **18**, 2069 (2003).
52. L. P. Sugrue, G. S. Corrado, W. T. Newsome, *Science* **304**, 1782 (2004).
53. M. L. Platt, P. W. Glimcher, *Nature* **400**, 233 (1999).
54. M. A. Belova, J. J. Paton, C. D. Salzman, *J. Neurosci.* **28**, 10023 (2008).
55. T. D. Hanks, J. Ditterich, M. N. Shadlen, *Nat. Neurosci.* **9**, 682 (2006).
56. A. C. Huk, M. N. Shadlen, *J. Neurosci.* **25**, 10420 (2005).
57. C. T. Law, J. I. Gold, *Nat. Neurosci.* **11**, 505 (2008).
58. A. Wald, *Sequential Analysis* (Wiley, New York, 1947).
59. D. R. J. Laming, *Information Theory of Choice Reaction Time* (Wiley, New York, 1968).
60. R. D. Luce, *Response Times: Their Role in Inferring Elementary Mental Organization* (Oxford University Press, Belfast, 1986).
61. D. M. Green, J. A. Swets, *Signal Detection Theory and Psychophysics* (Wiley, New York, 1966).
62. P. L. Smith, *J. Math. Psychol.* **32**, 135 (1988).
63. J. Gottlieb, *Neuron* **53**, 9 (2007).
64. E. T. Jaynes, *Probability Theory: The Logic of Science*, G. L. Bretthorst, Ed. (Cambridge University Press, Cambridge, 2003).
65. D. Howie, *Interpreting Probability: Controversies and Developments in the Early Twentieth Century* (Cambridge University Press, Cambridge, 2007).
66. D. C. Knill, A. Pouget, *Trends Neurosci.* **27**, 712 (2004).
67. R. S. Zemel, P. Dayan, A. Pouget, *Neural Comput.* **10**, 403 (1998).
68. This work was supported by the Howard Hughes Medical Institute, National Eye Institute grant EY11378, and National Center for Research Resources grant RR00166. We thank T. Hanks, A. Pouget, A. Churchland, D. Lee, P. Phillips, J. Palmer, and C. D. Salzman for helpful discussions and comments and A. Boulet and K. Ahl for technical assistance.

Supporting Online Material

www.sciencemag.org/cgi/content/full/324/5928/759/DC1
Materials and Methods
Figs. S1 to S4
Table S1
References

5 December 2008; accepted 11 March 2009
10.1126/science.1169405

REPORTS

Characterization of Multipartite Entanglement for One Photon Shared Among Four Optical Modes

Scott B. Papp,[1]* Kyung Soo Choi,[1]* Hui Deng,[2] Pavel Lougovski,[3] S. J. van Enk,[3] H. J. Kimble[1]†

Access to genuine multipartite entanglement of quantum states enables advances in quantum information science and also contributes to the understanding of strongly correlated quantum systems. We report the detection and characterization of heralded entanglement in a multipartite quantum state composed of four spatially distinct optical modes that share one photon, a so-called *W* state. By randomizing the relative phase between bipartite components of the *W* state, we observed the transitions from four- to three- to two-mode entanglement with increasing phase noise. These observations are possible for our system because our entanglement verification protocol makes use of quantum uncertainty relations to detect the entangled states that span the Hilbert space of interest.

Investigations of entanglement for two quantum systems have answered many fundamental questions in quantum physics (*1*, *2*) and revealed powerful new capabilities of quantum mechanics within the field of quantum information science (*3*–*5*). Many of these advances have used well-tested methods for the characterization of quantum entanglement in bipartite (two-component) systems (*6*, *7*). Entangled states of more than two systems enhance our knowledge of quantum theory, because new classes of states are available (*7*–*9*). Beyond applications to conventional quantum computation (*3*), exotic multipartite states have emerged as crucial resources for new directions in quantum information processing such as measurement-based quantum computation (*10*, *11*), quantum secret sharing (*12*), and quantum simulation (*13*). Despite the extraordinary promise that they offer, unambiguously detecting multipartite entangled states is still a major challenge from both an experimental and a theoretical standpoint.

Genuine N-partite entanglement is realized only with the simultaneous participation of all N of the constituent systems. The exponential increase with N in the amount of information required to describe the overall quantum system, although exceedingly beneficial for large-scale quantum information protocols (*3*), makes the task of classifying (*8*, *9*) and detecting such entangled states extremely difficult (*7*). Still, there are prescribed methods to detect entanglement in select classes of multipartite states that generally rely on reconstructing the density matrix $\hat{\rho}$. Linear entanglement witnesses supplemented by tomography of $\hat{\rho}$ have been used to detect entanglement in six (*14*) and eight (*15*) atomic ions, as well as for hyperentangled photons (*16*). A serious drawback of quantum-state tomography is the prohibitive number of measurements and their accuracies that are required with increasing N.

Our work focuses on a specific class of quantum states in which exactly one photon is coherently shared among N distinct optical modes in the form of

$$|W\rangle = \frac{1}{2}[(|1000\rangle + e^{i\phi_1}|0100\rangle) + e^{i\phi}(|0010\rangle + e^{i\phi_2}|0001\rangle)] \quad (1)$$

shown here for $N = 4$ and with the relative phases ϕ, ϕ_1, ϕ_2 of the modes. This is a so-called W state,

[1]Norman Bridge Laboratory of Physics 12-33, California Institute of Technology, Pasadena, CA 91125, USA. [2]Department of Physics, University of Michigan, Ann Arbor, MI 48109, USA. [3]Department of Physics, University of Oregon, Eugene, OR 97403, USA.

*These authors contributed equally to this work.
†To whom correspondence should be addressed. E-mail: hjkimble@caltech.edu

which plays an important role in quantum information protocols with photonic and matter qubits, because its entanglement is known to be robust against losses (for example, tracing over a set of modes $K \leq N-2$).

To detect entanglement for pure states in the form of Eq. 1 and their mixed-state counterparts $\hat{\rho}_W$, we introduce the use of fundamental quantum uncertainty relations. It has long been known for continuous variable systems that the uncertainty principle for noncommuting observables defines a boundary of measurement precision that can be crossed only by entangled states (*17*, *18*). This observation has formed the basis of numerous Einstein-Podolsky-Rosen–type experiments (*19*). For discrete variable systems as in Eq. 1, the uncertainty principle can be recast as a sum of uncertainties in certain physical observables that must always be greater than some minimum bound Δ_b for all unentangled states, whether pure or mixed (*20*).

As a first test of this concept, we created a bipartite entangled state analogous to $|W\rangle$. We verified the entanglement both by violation of an uncertainty relation (*21*) and by the well-established method of concurrence (*22*, *23*). The precise agreement of these two measurements over a wide range of parameter space attests to the reliability of uncertainty-based verification for the entanglement of discrete variables (Figs. 1B and 2). We then extended our setup to create multipartite entangled states that coherently share a single photon among four optical modes and applied our verification protocol to them. Varying the phase coherence and the photon statistics of a candidate state $\hat{\rho}_W$ allowed us to explore the boundary between separable and entangled states, including those that separate fourfold, threefold, and twofold entanglement.

Our verification protocol is based on an exclusion principle for which N-mode entanglement can be unambiguously detected by simultaneously measuring physical observables $\{\hat{M}_i\}$ (projectors) with $i \in \{1,\ldots,N\}$ more precisely than is possible with only $(N-1)$–mode entangled states and their mixtures (*20*, *21*). Specifically, we consider a sum uncertainty relation $\Delta = \sum_{i=1}^{N} \langle \hat{M}_i^2 \rangle - \langle \hat{M}_i \rangle^2 = 1 - \sum_{i=1}^{N} \langle \hat{M}_i \rangle^2$ and its lower boundary $\Delta_b^{(K)}$, which represents the smallest sum uncertainty obtained by any state with at most $K < N$–mode entanglement. For all K-mode entangled states, the inequality $\Delta \geq \Delta_b^{(K)}$ holds; therefore, a violation of this inequality serves as a sufficient condition for genuine N-mode entanglement. The projective operators are $\{\hat{M}_i\} = \{|W_i\rangle\langle W_i|\}$ with

$$
\begin{aligned}
|W_1\rangle &= \frac{1}{2}(|1000\rangle + e^{i\beta_1}|0100\rangle + \\
&\quad e^{i\beta_2}|0010\rangle + e^{i\beta_3}|0001\rangle) \\
|W_2\rangle &= \frac{1}{2}(|1000\rangle - e^{i\beta_1}|0100\rangle - \\
&\quad e^{i\beta_2}|0010\rangle + e^{i\beta_3}|0001\rangle) \\
|W_3\rangle &= \frac{1}{2}(|1000\rangle - e^{i\beta_1}|0100\rangle + \\
&\quad e^{i\beta_2}|0010\rangle - e^{i\beta_3}|0001\rangle) \\
|W_4\rangle &= \frac{1}{2}(|1000\rangle + e^{i\beta_1}|0100\rangle - \\
&\quad e^{i\beta_2}|0010\rangle - e^{i\beta_3}|0001\rangle) \qquad (2)
\end{aligned}
$$

for the case of $N = 4$, and with phases $\{\beta_j\}$ where $j \in \{1,2,3\}$. They are optimally sensitive to entanglement, for particular settings of β_j, because the entangled state $|W\rangle$ in Eq. 1 is the only simultaneous eigenstate of all projective operators $\hat{M}_i$ (*21*).

In our work, the purported N-mode entangled state $\hat{\rho}_W$ analogous to $|W\rangle$ is generated via the operation $\hat{\rho}_{in} \xrightarrow{\hat{U}_{gen}} \hat{\rho}_W$ (Fig. 1A) on an input state $\hat{\rho}_{in}$. Similarly, entanglement is verified with

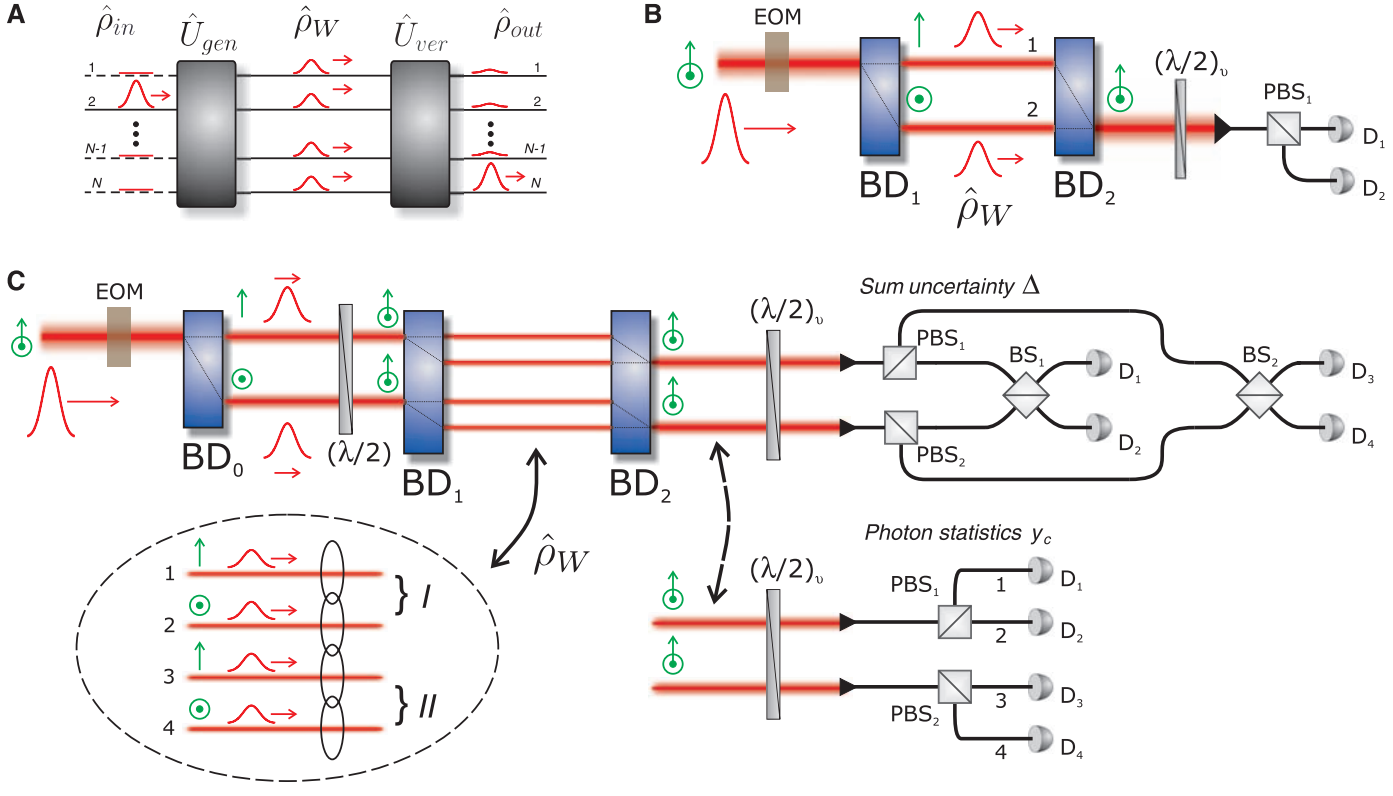

Fig. 1. Diagram of our entanglement generation and verification setups. (**A**) A single-photon pulse is transformed from a single input into an N-mode entangled state by $\hat{U}_{gen}$, and entanglement is verified with the operation $\hat{U}_{ver}$. (**B**) Details of the setup for bipartite entanglement. Single photons are coherently split to occupy the two modes defined by the interferometer BD_1-BD_2 with the relative phase ϕ of $\hat{\rho}_W$ controlled by the EOM. By setting the waveplate $(\lambda/2)_v$ at 0°, the occupation of the individual modes is detected at D_1 and D_2, and we obtain the two-photon components of $\hat{\rho}_W$. With a setting of $(\lambda/2)_v$ at 22.5°, single-photon interference occurs at PBS_1, from which we obtain Δ; see also Fig. 2. (**C**) Details of the setup to create and verify quadripartite entanglement. The sequences of beamsplitters BD_0 and BD_1 generate the optical modes 1 to 4, which share a single photon. To measure Δ, we jointly optimized the relative phases in the verification interferometers for interferences at $PBS_{1,2}$ [$(\lambda/2)_v$ at 22.5°] and $BS_{1,2}$ to minimize the photon probability of all but one output mode. Here, switching between measurements of Δ and y_c requires the indicated reconfiguration of fiber-optic components.

$\hat{\rho}_W \xrightarrow{\hat{U}_{\mathrm{var}}} \hat{\rho}_{\mathrm{out}}$. We implemented $\hat{M}_i$ for the case of two (Fig. 1B) and four (Fig. 1C) optical modes using beamsplitters (*24*) and photodetectors. The limit $\Delta \to 0$ indicates a significant overlap of the state $\hat{\rho}_W$ with only one of the projectors $\hat{M}_i$. In particular, for any choices of ϕ, ϕ_1, ϕ_2 that define Eq. 1 and the three corresponding orthonormal states, our measurements of $\hat{M}_i$ would yield $\Delta = 0$ for optimal settings of the phases β_j. A small Δ corresponds to a large statistical imbalance in the event distribution of the output optical modes, with one mode strongly preferred over the others. Conversely, if the generated state contains a photon that occupies one mode (e.g., $|1000\rangle$), our measurements would yield $\Delta = 0.75$. Because of the presence of transmission losses and beamsplitter imbalances in our setups, the projectors $|W_i\rangle\langle W_i|$ evolve into mixed states with significant vacuum components, but genuine multipartite entanglement can still be robustly detected for $\hat{\rho}_W$ (*21*, *25*).

To theoretically determine the boundaries $\Delta_b^{(K)}$ for N-mode entanglement, we calculated Δ for all possible admixtures of states containing at most $K = N - 1$–mode entanglement. The presence of more than one excitation in $\hat{\rho}_W$ may allow significant overlap of its one-photon subspace with $|W\rangle$, leading to a spurious detection of entanglement. Therefore it is necessary to determine the contamination of the state $\hat{\rho}_W$ caused by multiple excitations. By invoking local filtering operations, we are justified in confining our analysis to the reduced-density matrix $\hat{\rho}_W^{(r)} = p_0\hat{\rho}_0 + p_1\hat{\rho}_1 + p_{\geq 2}\hat{\rho}_{\geq 2}$, which contains no more than one photon per mode, while still being guaranteed a lower bound of entanglement (*6*, *23*). In our experiments, we measured the photon probabilities p_0, p_1, and $p_{\geq 2}$ that characterize the occupation of the vacuum subspace $\hat{\rho}_0$, the single-photon subspace $\hat{\rho}_1$, and the subspace containing multiple excitations $\hat{\rho}_{\geq 2}$. The degree of contamination due to more than one excitation is quantified by the parameter $y_c = 2\left(\frac{N}{N-1}\right)\frac{p_2 p_0}{p_1^2}$, which is normalized to the case of independent and balanced coherent states for which $y_c = 1$. The observation of measurement uncertainty Δ below the threshold $\Delta_b^{(K)}$ together with a determination of y_c, then, manifestly confirms the presence of genuine $(K + 1)$–mode entanglement.

Our experimental starting point was the generation of heralded single photons via Raman transitions in an optically dense atomic ensemble of Cs atoms (*25*, *26*). Two-mode entangled states were created by coherently splitting a single photon into parallel modes with beam displacer BD_1 (Fig. 1B); the modes' relative phase, analogous to ϕ in Eq. 1, was controlled by an electro-optic modulator (EOM). The spatially separated modes were recombined at BD_2 and coupled into a single-mode optical fiber, with each mode encoded in the polarization bases $|H\rangle$ and $|V\rangle$. Achieving entanglement requires a constant relative phase of the optical modes. In the absence of any fluctuating drive voltage on the EOM, the beam displacer pair BD_1-BD_2 forms a passively stable interferometer (*27*). By driving the EOM with a randomly oscillating voltage, the phase coherence of the modes is destroyed, and any entanglement between them is lost. This setup provides a calibrated tool to explore the boundary between separable and entangled states.

After the generation of bipartite states, we searched for the signatures of entanglement, using our verification protocol. To measure Δ, we rotated the polarizations of both modes by 45° and interfered them with a polarizing beamsplitter (PBS_1). We recorded the photoelectric detection events at single-photon counters D_1 and D_2, and converted them to the normalized joint photon probabilities P_{ij} (i.e., i photons for mode 1 and j for mode 2). Varying the relative phase of the modes after they exit BD_2 produces the interference fringes shown in Fig. 2A′ (corresponding to P_{10} and P_{01}), which allow us to identify the minimum value of Δ supported by the modes for a given y_c. In particular, the sum uncertainty Δ is related to the fringe visibility V by $\Delta = \frac{1}{2}(1 - V^2)$. When the relative phase β between modes 1,2 is either 0° or 180°, we obtain a value of Δ as small as 0.006, which corresponds to a visibility of 99.4% (*25*). To measure the two-photon suppression of $\hat{\rho}_W$, we detected the individual modes and recorded the time series of all relevant coincidence events (i.e., P_{ij} with $\{i,j\} \in \{0, 1\}$). Based on a calibration of the transmission from the face of BD_2 to the detectors, we inferred the photon probabilities that determine y_c (*25*). We controlled y_c via the pump intensity for Raman transitions in the source ensemble (*25*).

We have explored bipartite entanglement verification in our system by varying both the phase coherence and the two-photon suppression of $\hat{\rho}_W$. Figure 2A shows the dependence of Δ on the amplitude $\delta\phi$ of phase noise produced by the EOM. These results were obtained with two-photon contamination $y_c = 0.063 \pm 0.011$, so that entanglement is detected when $\Delta \lesssim 0.46$. With $\delta\phi = 360°$, we expect the fringe visibility to be minimized, and therefore $\Delta = 0.5$. As $\delta\phi$ decreases below 270°, the statistics of our measurements become sufficiently imbalanced that the presence of entanglement is manifest. Without any phase noise in the state generated at BD_1 (i.e., $\delta\phi = 0$), we obtain $\Delta \leq 0.03$ over a wide range of y_c as shown in Fig. 2B. The first-order coherence of our single-photon source and the phase stability of our apparatus guarantee $\Delta \approx 0$. The boundary in Δ between fully separable states and those that contain entanglement, $\Delta_b^{(1)}$, depends primarily on y_c through the rela-

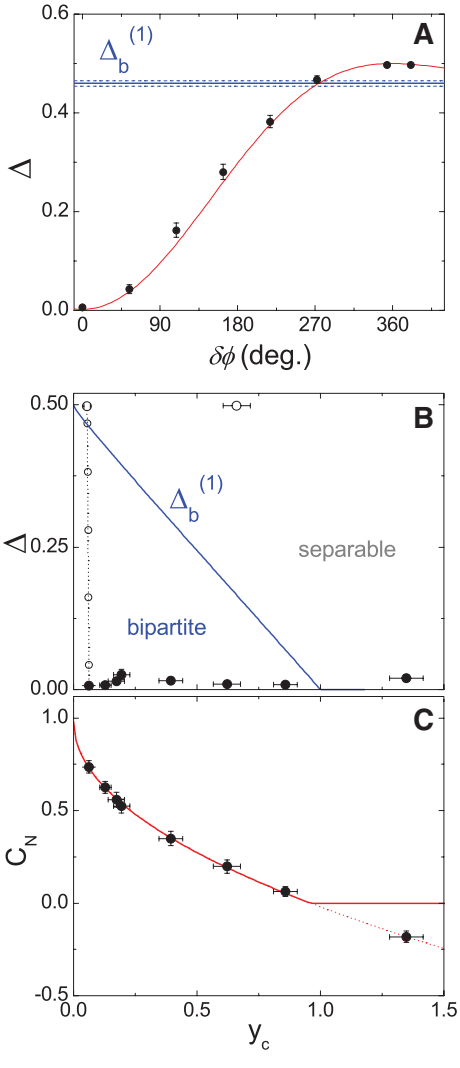

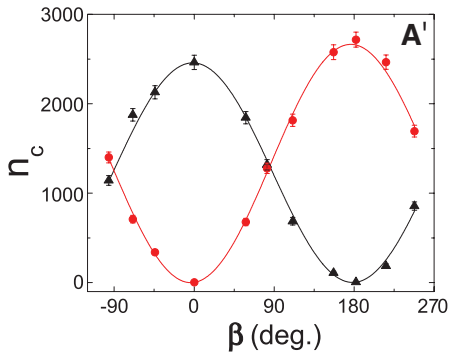

Fig. 2. Detection of entanglement between two optical modes using uncertainty relations. (**A**) The sum uncertainty Δ as a function of peak-to-peak phase noise $\delta\phi$ in the generated state $\hat{\rho}_W$. The solid blue line gives the boundary, $\Delta_b^{(1)}$, between entangled and separable states. The dotted blue lines indicate the range of $\Delta_b^{(1)}$ values that result from the uncertainty in our measurements of y_c. The red line is a fit to the data, based on a uniform distribution of phase noise. (**A′**) Number of photons detected n_c in the output modes for a measurement time of 250 s as the relative phase β of the verification interferometer is varied. At minima and maxima of n_c, we obtain $\Delta = 0.01$. (**B**) Measured sum uncertainty with $\delta\phi = 0$ (solid circles) and boundary $\Delta_b^{(1)}$ (blue line) as a function of two-photon suppression. Data with $y_c < 1.0$ demonstrate entanglement of the two modes. By variation of $\delta\phi$ from 0° to 360° (open circles), the modes' phase coherence is reduced, resulting in a loss of entanglement for $\delta\phi \gtrsim 270°$. (**C**) Concurrence C_N (filled circles) inferred from measurements of Δ and the boundary $\Delta_b^{(1)}$. The solid line shows a theoretical prediction of concurrence $[\max(C_N,0)]$ based on an independent measurement of V and $p_1 = 0.22 \pm 0.02$. All the error bars in this figure represent standard deviations.

tion $\Delta_b^{(1)} = \frac{1}{2}(1 - y_c)$. Given the uncertainty of our measurements, of which the largest contribution is counting fluctuations in y_c, all of the states created with $y_c \leq 0.86$ verifiably contain entanglement.

A rigorous correspondence exists between our uncertainty verification protocol (for two modes) and concurrence, a measure of bipartite entanglement (*22*, *25*). As a tool to understand the dependencies of the sum uncertainty and as a secondary confirmation of two-mode entanglement, we inferred the (normalized) concurrence $C_N = V - \sqrt{y_c}$ from our measurements of Δ. Using previously introduced relations, we can reformulate it as $C_N = \sqrt{1 - 2\Delta} - \sqrt{1 - 2\Delta_b^{(1)}}$. The inferred concurrence data shown in Fig. 2C demonstrate an increasing C_N, therefore a larger degree of entanglement, as we decrease y_c. This behavior is in excellent quantitative agreement with our theoretical expectation for concurrence based on quantum-state tomography (*23*, *25*); this validates the use of uncertainty relations for entanglement verification.

We now describe our investigation of multipartite entanglement with a single photon shared among four optical modes (Figs. 3 and 4). To generate four-mode entangled states, we used the setup shown in Fig. 1C. A third beam displacer (BD_0) was added to the two-mode setup immediately before BD_1; it coherently splits a single photon polarized at 45° into two modes. In this case, the space between BD_1 and BD_2 supports four independent modes of $\hat{\rho}_W$ (composed of pairs *I* and *II*) that share a single photon. The EOM influences only the relative phase of the two pairs *I*, *II*, labeled ϕ in Eq. 1, leaving intact their individual phase coherence; and it provides a means to induce dephasing between the *I*, *II* pairs. The four spatially separated modes in the state $\hat{\rho}_W$ are combined into two separated spatial modes (each carrying two modes encoded via the polarizations $|H\rangle$ and $|V\rangle$) that exit BD_2 and are coupled into single-mode fibers.

Measurements of Δ were performed by rotating the polarizations of all the modes by 45° and pairwise interfering them with the network of four cascaded beamsplitters shown in Fig. 1C. We recorded all photoelectric events from detectors $\{D_1,...,D_4\}$, but employed only events with a single photodetection for the determination of Δ (*25*). In this case, Δ depends jointly on the fringe visibilities of all four interferometric outputs. BD_1 and BD_2 still guarantee long-term interferometric stability for the two pairs of modes *I* and *II*, and the relative phases between other pairs are actively stabilized with respect to a laser that shares the same path. With the stabilization laser off, we applied calibrated feed-forward signals to the servo electronics, that transiently optimized the setup for measurements of various phase dependencies of Δ, including its global minimum (*25*). To extract y_c for the separated modes 1 to 4, we inserted the "photon statistics" setup at the location indicated in Fig. 1C, and we ensured that no interference occurred at PBS_1 and PBS_2 by setting the polarizations to the eigenaxes of the respective PBS. We obtained a record of the 16 photon probabilities P_{ijkl} that determine y_c, with indices $i, j, k, l \in \{0, 1\}$ (*25*).

Using sum uncertainty relations (*20*, *21*), we have unambiguously detected the presence of full four-mode entanglement in a photonic *W* state. Because $N > 2$, entanglement may be found not only among the full set of modes, but bipartite- and tripartite-entangled states exist within a subset of them. A crucial feature of our verification protocol is that it clearly defines boundaries that distinguish between states with $\{N, N-1,..., 2\}$–mode entanglement. As in the case with $N = 2$, the boundaries for $N = 4$ exist within the parameter space defined by Δ and y_c. To understand how the multipartite entanglement is affected by the phase coherence of $\hat{\rho}_W$, we introduced phase noise δϕ over the range from 0° to 360° between the two pairs of modes. Figure 3 shows Δ as a function of δϕ and the theoretical boundaries for two-, three-, and four-mode entanglement. For $\delta\phi \leq 225°$, our verification protocol confirmed the presence of genuine multipartite entanglement for three and four modes. Owing to the fact that dephasing was induced among only two pairs, the measured sum uncertainties do not exceed the threshold $(\Delta_b^{(1)} = 0.7)$ defined by fully separable states. A primary feature of multipartite *W* states is their resilience against phase noise, evidenced by the

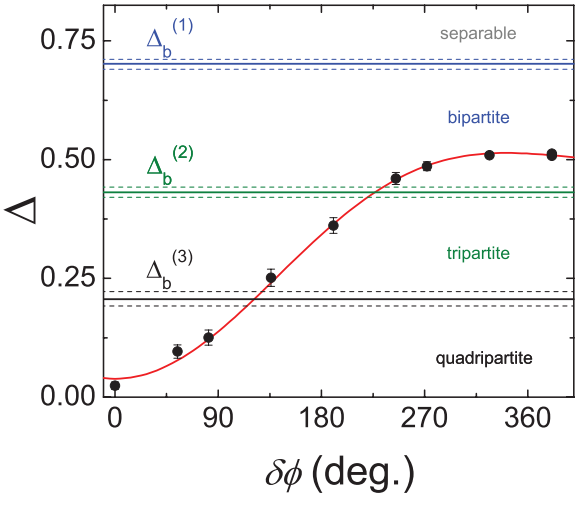

Fig. 3. Dependence of the sum uncertainty Δ on the amplitude of phase noise δϕ in the state $\hat{\rho}_W$. These data were acquired with an approximately constant y_c in the range from 0.06 to 0.08; under these conditions, $\Delta \lesssim 0.2$ demonstrates genuine four-mode entanglement. The horizontal lines indicate the boundaries $\Delta_b^{(K)}$ for entanglement. Here the uncertainty of each boundary $\Delta_b^{(K)}$ (dashed lines) corresponds to the observed fluctuations in y_c. The red line is a fit to the data, based on a model including a uniform distribution of phase noise.

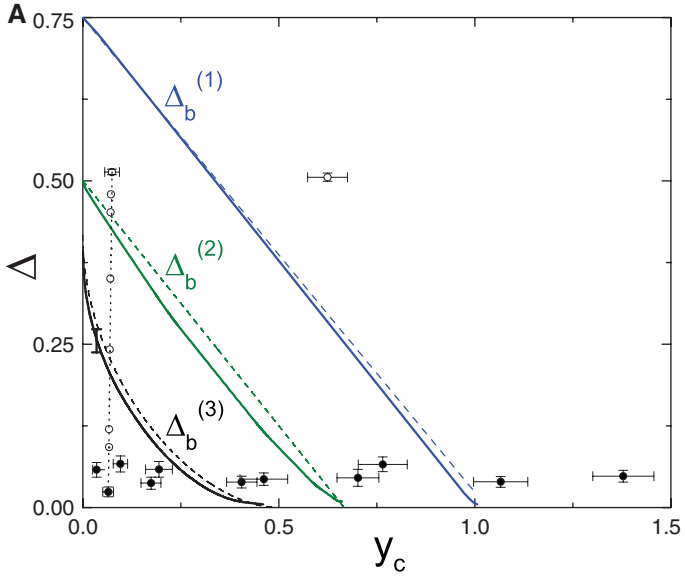

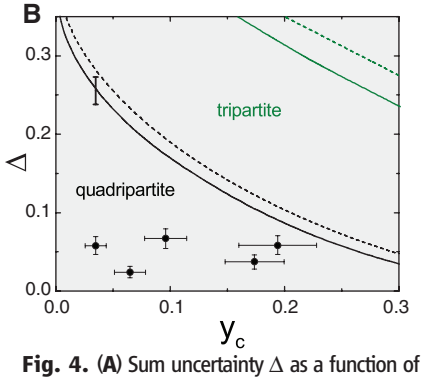

Fig. 4. (**A**) Sum uncertainty Δ as a function of two-photon suppression for $\delta\phi = 0°$ (solid circles) and $\delta\phi = 0°$ to 360° (open circles). Solid lines indicate the boundaries between separable, bipartite-, and tripartite-entangled states for the parameters of our experiment. To indicate the sizes of boundary corrections from the ideal case, the dashed lines show $\Delta_b^{(K)}$ for the ideal balanced and lossless case. The error bar on $\Delta_b^{(3)}$ indicates the statistical uncertainty in the boundary (*25*). (**B**) An expanded view of the quadripartite sector.

fact that the state that results from tracing over two modes in Eq. 1 still remains two-mode entangled (*28*). This property of $|W\rangle$ explains our observation of entanglement even in the face of complete dephasing between pairs *I* and *II* with 360° of phase noise.

We have also explored the transitions from fully separable to bipartite ($K = 1$), tripartite ($K = 2$), and quadripartite ($K = 3$) entangled W states by measuring the sum uncertainty as a function of two-photon suppression y_c, with our results presented in Fig. 4. With $\delta\phi = 0$, we obtained a uniformly low $\Delta \leq 0.08$ over a range in y_c from 0.035 to 1.37. These values of Δ are larger than in the two-mode case (Fig. 2B) and are explained by a small imbalance in $\hat{\rho}_W$ and by imperfections in the entanglement verification interferometers. Furthermore, these imperfections play an important role in the determination of the boundaries $\Delta_b^{(K)}$ for entanglement. As detailed in (*25*), small imbalances in the beamsplitter ratios of $PBS_{1,2}$ and $BS_{1,2}$ in Fig. 1C, and nonbalanced transmission losses lead to displacements of the boundaries toward smaller Δ, y_c. To reduce these boundary corrections, the beamsplitter ratios were all matched to 50%/50% to less than 3%, and the difference in losses of corresponding free-space and in-fiber optical paths were always held to less than 4%. Figure 4 shows the sizes of the corrections by displaying the boundaries $\Delta_b^{(K)}$ for the ideal lossless and balanced case as dashed lines.

In comparison to quantum-state tomography, our multipartite verification protocol features an exponential reduction in the number of measurements required to unambiguously detect entanglement. Specifically, our protocol requires us to determine 2^4 elements of $\hat{\rho}_W^{(r)}$ for y_c and 4 elements of $\hat{U}_{ver}^{\dagger}\hat{\rho}_W^{(r)}\hat{U}_{ver}$ for Δ, a total of 20 elements out of the $4^4 = 256$ that make up the reduced-density matrix $\hat{\rho}_W^{(r)}$. Our protocol inherently features the use of nonlocal measurements $\hat{M}_i$, thereby requiring only two experimental steps to measure all necessary elements and unambiguously detect entanglement in $\hat{\rho}_W$. Furthermore, the nonlinear structure of Δ allows the simultaneous detection of all possible realizations of Eq. 1 (*7*, *21*). These features alleviate the need for any complicated mechanism to control the measurement basis, which can be a challenge in tomography experiments (*16*) and other local measurement–based verification protocols for $\hat{\rho}_W$. Although linear witnesses might also enable entanglement detection with less than full knowledge of $\hat{\rho}_W$ obtained from a few experimental steps (*29*), the unambiguous verification of entanglement requires robustness in the face of experimental imperfections, including multiple excitations and losses (*25*).

Our study has introduced a new technique for the unambiguous verification of multipartite W states. Specifically, we examined entanglement in heralded quantum states specified by $\hat{\rho}_W$ with $N = 2,4$. Entanglement detected with our protocol refers to that of the complete density matrix $\hat{\rho}_W$ presented to our verification system, and not to fictitious components deduced via post selection (*6*). An extension of our protocol to different states (requiring increased experimental resources) is discussed in (*21*). Photonic entanglement, such as generated here, can be coherently mapped into atomic memories by way of electromagnetically induced transparency (*30*) for scalable quantum networks.

References and Notes

1. J. F. Clauser, A. Shimony, *Rep. Prog. Phys.* **41**, 1881 (1978).
2. A. Aspect, P. Grangier, G. Roger, *Phys. Rev. Lett.* **47**, 460 (1981).
3. M. A. Nielsen, I. L. Chuang, *Quantum Computation and Quantum Information* (Cambridge Univ. Press, Cambridge, 2000).
4. P. Zoller *et al.*, *Eur. Phys. J. D* **36**, 203 (2005).
5. H. J. Kimble, *Nature* **453**, 1023 (2008).
6. S. J. van Enk, N. Lütkenhaus, H. J. Kimble, *Phys. Rev. A* **75**, 052318 (2007).
7. O. Gühne, G. Toth, preprint available at http://arxiv.org/abs/0811.2803v2 (2008).
8. W. Dur, G. Vidal, J. I. Cirac, *Phys. Rev. A* **62**, 062314 (2000).
9. F. Verstraete, J. Dehaene, B. De Moor, H. Verschelde, *Phys. Rev. A* **65**, 052112 (2002).
10. R. Raussendorf, H. J. Briegel, *Phys. Rev. Lett.* **86**, 5188 (2001).
11. E. Knill, R. Laflamme, G. J. Milburn, *Nature* **409**, 46 (2001).
12. M. Hillery, V. Buźek, A. Berthiaume, *Phys. Rev. A* **59**, 1829 (1999).
13. S. Lloyd, *Science* **273**, 1073 (1996).
14. D. Leibfried *et al.*, *Nature* **438**, 639 (2005).
15. H. Haffner *et al.*, *Nature* **438**, 643 (2005).
16. W.-B. Gao *et al.*, preprint available at http://arxiv.org/abs/0809.4277v1 (2008).
17. L.-M. Duan, G. Giedke, J. I. Cirac, P. Zoller, *Phys. Rev. Lett.* **84**, 2722 (2000).
18. R. Simon, *Phys. Rev. Lett.* **84**, 2726 (2000).
19. S. L. Braunstein, P. van Loock, *Rev. Mod. Phys.* **77**, 513 (2005).
20. H. F. Hofmann, S. Takeuchi, *Phys. Rev. A* **68**, 032103 (2003).
21. P. Lougovski *et al.*, preprint available at http://arxiv.org/abs/0903.0851v1 (2009).
22. W. K. Wootters, *Phys. Rev. Lett.* **80**, 2245 (1998).
23. C. W. Chou *et al.*, *Nature* **438**, 828 (2005).
24. M. Reck, A. Zeilinger, H. J. Bernstein, P. Bertani, *Phys. Rev. Lett.* **73**, 58 (1994).
25. See the supporting material on *Science* Online.
26. L.-M. Duan, M. D. Lukin, J. I. Cirac, P. Zoller, *Nature* **414**, 413 (2001).
27. C.-W. Chou *et al.*, *Science* **316**, 1316 (2007).
28. C. F. Roos *et al.*, *Science* **304**, 1478 (2004).
29. H. Nha, *Phys. Rev. A* **77**, 062328 (2008).
30. K. S. Choi, H. Deng, J. Laurat, H. J. Kimble, *Nature* **452**, 67 (2008).

31. We gratefully acknowledge critical discussions with J. Laurat, P. Zoller, and J. Ye. This research is supported by IARPA, by NSF, and by NGST. S.P. and H.D. acknowledge support as Fellows of the Center for the Physics of Information at Caltech.

Supporting Online Material

www.sciencemag.org/cgi/content/full/324/5928/764/DC1
Methods
SOM Text
Figs. S1 to S5
Table S1
References

13 February 2009; accepted 18 March 2009
10.1126/science.1172260

N-Doping of Graphene Through Electrothermal Reactions with Ammonia

Xinran Wang,[1] Xiaolin Li,[1] Li Zhang,[1] Youngki Yoon,[2] Peter K. Weber,[3] Hailiang Wang,[1] Jing Guo,[2] Hongjie Dai[1]*

Graphene is readily p-doped by adsorbates, but for device applications, it would be useful to access the n-doped material. Individual graphene nanoribbons were covalently functionalized by nitrogen species through high-power electrical joule heating in ammonia gas, leading to n-type electronic doping consistent with theory. The formation of the carbon-nitrogen bond should occur mostly at the edges of graphene where chemical reactivity is high. X-ray photoelectron spectroscopy and nanometer-scale secondary ion mass spectroscopy confirm the carbon-nitrogen species in graphene thermally annealed in ammonia. We fabricated an n-type graphene field-effect transistor that operates at room temperature.

Recently, graphene has been made into semiconductors in the form of nanoribbons, leading to room temperature p-type graphene field-effect transistors (FETs) (*1*, *2*). However, a fundamental problem has been that the edge structures and chemical terminations of graphene synthesized by various methods are unknown and uncontrolled, whereas their effects to the physical properties have been widely predicted (*3*–*9*). In particular, graphene nanoribbons (GNRs) edge-terminated by nitrogen species were shown to be electron-rich, leading to n-type transistor behavior (*8*). Therefore, it is essential to precisely control the edge structures and chemical terminations to obtain desirable device characteristics. Edge doping could present a new means of doping for nanoscale graphene.

We now report that GNRs can be functionalized by nitrogen species by high-power electrical annealing (e-annealing) in NH_3 and exhibit n-type electronic doping. GNRs were synthesized chemically (*1*) or were lithographically patterned from pristine peel-off graphene (*10*–*12*); the

[1]Department of Chemistry and Laboratory for Advanced Materials, Stanford University, Stanford, CA 94305, USA. [2]Department of Electrical and Computer Engineering, University of Florida, Gainesville, FL 32611, USA. [3]Chemical Sciences Division, Lawrence Livermore National Laboratory (LLNL), Livermore, CA 94550, USA.

*To whom correspondence should be addressed. E-mail: hdai@stanford.edu